PAPER

Biomimicking interfacial fracture behavior of lizard tail autotomy with soft microinterlocking structures

To cite this article: Navajit S Baban *et al* 2022 *Bioinspir. Biomim.* **17** 036002

View the article online for updates and enhancements.

Bioinspiration & Biomimetics

Biomimicking interfacial fracture behavior of lizard tail autotomy with soft microinterlocking structures

Navajit S Baban[1] , Ajymurat Orozaliev[1], Christopher J Stubbs[2] and Yong-Ak Song[1,3,4,*]

[1] Division of Engineering, New York University Abu Dhabi, Abu Dhabi, United Arab Emirates
[2] Gildart Haase School of Computer Science and Engineering, Fairleigh Dickinson University, Teaneck, NJ 07666, United States of America
[3] Department of Chemical and Biomolecular Engineering, Tandon School of Engineering, New York University, NY, United States of America
[4] Department of Biomedical Engineering, Tandon School of Engineering, New York University, NY, United States of America
[*] Author to whom any correspondence should be addressed.

E-mail: rafael.song@nyu.edu

Abstract

Biological soft interfaces often exhibit complex microscale interlocking geometries to ensure sturdy and flexible connections. If needed, the interlocking can rapidly be released on demand leading to an abrupt decrease of interfacial adhesion. Here, inspired by lizard tail autotomy where such apparently tunable interfacial fracture behavior can be observed, we hypothesized an interlocking mechanism between the tail and body based on the muscle-actuated mushroom-shaped microinterlocks along the fracture planes. To mimic the fracture behavior of the lizard tail, we developed a soft bilayer patch that consisted of a dense array of soft hemispherical microstructures in the upper layer acting as mechanical interlocks with the counter body part. The bottom control layer contained a microchannel that allowed to deflect the upper layer when applying the negative pressure, thus mimicking muscle contraction. In the microinterlocked condition, the biomimetic tail demonstrated a 2.7-fold and a three-fold increase in adhesion strength and toughness, respectively, compared to the pneumatically released microinterlocks. Furthermore, as per the computational analysis, the subsurface microchannel in the control layer enabled augmented adhesion by rendering the interface more compliant as a dissipative matrix, decreasing contact opening and strain energy dissipation by 50%. The contrasting features between the microinterlocked and released cases demonstrated a highly tunable adhesion of our biomimetic soft patch. The potential applications of our study are expected in soft robotics and prosthetics.

1. Introduction

In nature, biological interfaces often exhibit complex microscale sutured or form-based microinterlocked geometries critical for ensuring sturdy but flexible connectivity while providing multiple essential functionalities [1–5] such as respiration, growth, and locomotion of organisms. These microinterlocked interfaces significantly increase the associated stiffness and strength due to the related strengthening and toughening mechanisms such as crack propagation hindrance [2, 5, 6], mode-mixity [1, 6, 7], extended energy dissipation zone [8], and friction interaction [9]. Also, the extrinsic (behind crack tip) [10]

toughening mechanisms and intrinsic (ahead of the crack tip) [10] toughening mechanisms such as crack deflection or kinking [5, 7], stick-slip [11] response, and microvoid coalescence [10] contribute significantly towards the damage tolerance of the nature-designed interfaces. These toughening strategies have been well studied and exploited to increase interlayer performance in composites [12] and biomimetic artificial interfaces for various technical applications [2, 6, 10]. Conversely, *in situ*, the interlayer adhesion could significantly decrease when detaching these interlocks by rapid actuation on-demand, enabling a high-end tunable interlayer adhesion.

Recent progress in the development of application-oriented tunable adhesion has been made using bioinspiration from gecko seta [13, 14], creeper root [15], octopus [16], temperature-induced [15, 17], shape-controlled caps [18], magnetically-tuned micropillar rotation [19], subsurface pressure modulation [20], dewetting modification [21], and swellable hydrogel [22]. Despite the significant progress made, there are still challenges to implement mechanically interlocking structures that simultaneously allow for sturdy and flexible connection and on-demand rapid detachment. In this paper, we present a tunable adhesion approach bioinspired from lizard tail autotomy.

Lizard tail autotomy (self-amputation) is a unique survival strategy used by lizards for predator defense where the mechanical release of the tail facilitates escape [23, 24]. After the tail is released, it continues to wiggle on its own to attract the predator's attention while the lizard escapes. Interestingly, the lizard tail is not a single entity; instead, it consists of several segments that are assembled to each other, constituting fracture planes [25]. Inspired by the tail's morphology and the highly dense mushroom-shaped microstructures present on the fracture planes during SEM analysis, we developed a biomimetic approach to tunable adhesion between soft layers using pneumatically actuated microinterlocking structures via a two-layer polydimethylsiloxane (PDMS) patch. The top layer of the patch consisted of a square array of ∼12 000 hemispherical microstructures (∼50 μm diameter and height) called the microbump layer. These flexible microstructures acted as an array of mechanical interlocks with the counter body part that can be disconnected by pneumatic actuation via a subsurface microfluidic channel in the bottom control layer. Fracture characterizations validated a significant change in fracture strength and toughness before and after actuation compared to the planar reference [26].

2. Methods

2.1. Scanning electron microscopy of lizard tail specimen

We studied the tails of three common lizard species from Abu Dhabi, two from the Gekkonidae family (*Hemidactylus flaviviridis* and *Cyrtopodion scabrum*) as well as one from the Lacertidae family (*Acanthodactylus schmidti*). Animal care protocols were approved by the Institutional Animal Care and Use Committee (IACUC; Laboratory animal protocol 20-0002), as well as a no-objection certificate (NOC), was obtained by the Environment Agency Abu Dhabi (EAD; No Objection Certificate Number 34867). The tail fragments were immediately preserved in a 4% formalin fixative after breakage, which was subsequently stored at 4 °C.

For scanning electron microscopy (SEM), the 4% formalin-fixed tail fragments were washed three times (with a 10 min gap between the washes) with 0.1 M sodium cacodylate buffer. Post washing, the specimens were kept in 1% OsO_4 for 2 h. Then, the specimens were washed with distilled water three times (with 10 min gap between the washes). The specimens were dehydrated by subjecting them to a graded ascending ethanol series with concentrations of 50%, 70%, 95%, and 100%, all following the same scheme of three washing steps with a 10 min gap in between. The resulting specimen was critical point dried using a Leica CPD apparatus (Leica EM CPD300, Leica Inc.). The tail stump specimens were glued on a stub and coated with a 20 nm gold layer using a sputterer before performing the SEM.

2.2. Master mold fabrication

A 4″ silicon wafer was baked at 150 °C using a leveled hotplate for 5 min to remove the adsorbed layer of water from the surface. Then, the adhesion promoter TI PRIME was spin-coated at 2000 rpm for 30 s, followed by subsequent baking at 120 °C for 2 min to activate the adhesion promoter. The photoresist AZ40XT was spin-coated at 1000 rpm for 30 s immediately after the wafer was cooled down to room temperature. Once cooled down to room temperature after 20 min, it was subjected to soft baking on a hotplate for 7 min with ramp heating (50 °C–90 °C). It was transferred to a second hotplate at 125 °C for 11 min and then cooled down. Finally, the wafer was exposed to UV using a mask aligner (MA8, SUSS). After exposure, post-exposure baking was performed with ramp heating (50 °C–90 °C), and the master was then transferred to the second hotplate at 105 °C for 100 s. It was then cooled down to room temperature for 10 min. After development in undiluted AZ326MIF for 3 min and 25 s, the photoresist was thermally reflown at 130 °C for 2 min to obtain the array of hemispherical microstructures on the patch area. The size of each microstructure was approximately equal to 50 μm in diameter. The fabrication process is schematically shown in supplementary figure 1 (https://stacks.iop.org/BB/17/036002/mmedia).

The microchannels of the control layer were fabricated using soft lithography. Briefly, a negative photoresist SU8-2050 was used to create a master mold with a channel dimension of ∼100 μm × 100 μm. The PDMS microchannels were obtained from the SU-8 master by molding. The microbump and control layers were plasma bonded together for a watertight connection to deflect the microbump layer using pneumatic suction in the control layer.

2.3. Fabrication of tail and body part

For the tensile and torque experiments, we built a rigid and soft tail, respectively. The biomimetic tail and the body mount were modeled using

Solidworks® 2017 and 3D printed using Formiga P 100 Velocis 3D printer. The material used for 3D printing was polyamide, PA 1102 (Young's modulus = 1600 MPa and density 990 kg m^{-3}).

Before connecting the body and tail, the two-layer PDMS patches were first silanized using trichloro (1H, 1H, 2H, 2H,—perfluoro—octyl) silane that formed a self-assembled inert monolayer on the surface. The silanized patches were then attached to the V-shaped fracture planes of the tail using liquid PDMS with a curing agent (10:1) that acted as a glue post-curing at 70 °C for 30 min. After filling the gap (5 mm) between the body and the silanized PDMS patches with uncured PDMS and subsequent curing, a layer with precisely aligned complementary microgrooves was formed on the soft body part against the microbumps of the PDMS patches. Furthermore, to enable a firm connection of the soft body part (with the complementary microgrooves) to the body mount, dumbbell-shaped pockets were additionally provided in the body mount. Supplementary text 1 schematically shows the above fabrication process.

For the flexible tail (see supplementary figure 2, EcoFlex® 00-20 tail was fabricated using a Teflon mold, which was designed with Solidworks® 2017 and machined by computer numerical control milling. A mixture of EcoFlex® 00-20 part A and part B was poured into the mold and left to cure in the oven at 70 °C for 30 min. Similar to the rigid tail, the silanized PDMS patches were bonded to the V-shaped fracture planes and connected to the 3D printed body mount by filling liquid EcoFlex® 00-20 plus curing agent into the gap (5 mm) between the body part and the silanized PDMS patches and subsequently curing them at 70 °C for 30 min. The fabrication process of the rigid and flexible tail is explained in supplementary text 1 in detail. Finally, post-experiment SEM analysis was conducted along the broken fracture planes to validate interfacial fracture between the body and tail.

2.4. Experimental design and set-up

The test samples had three different topological features on the fracture planes, namely plain (reference), non-actuated (with engaged microinterlocks), and actuated samples (with released microinterlocks). For comparison, all the test samples incorporated an embedded subsurface microchannel in the control layer, including the plain (reference). The control layer was subjected to a negative pressure of −1000 mbar so as to deflect the microbump layer and break the microinterlocks. As a pressure source, a pressure pump (Elveflow®) [27] was connected to the PDMS patch via soft tubing. Using a universal testing machine (Instron® 5965, Instron Corp., Norwood, MA, USA), the force required to break apart the tail from the body was measured for different samples at various displacement rates. To avoid any possible

interference of wavy fingerlike debonding concerning fracture characterization results, the interface was monitored under an optical microscope during fracture. The outcome recorded, no signs of wavy fingerlike instabilities that would have confounded the results if present (supplementary text 2. Next, fracture characterizations were performed in tensile and torque modes. The procedure and the details about the tensile and torque mode of the fracture tests are given below.

The sample tail's body mount was fixed using the bottom grip, and with the help of the top grip, the tail was displaced at various displacement rates depending on the fracture mode of the test. Loads were measured with a 500 N Instron load cell (load accuracy of ±5%) at a displacement rate of 5 μm s^{-1} for the tensile fracture experiment and 5 mm s^{-1} for the torque fracture experiment. The load cell was calibrated with the no-load mounted condition before the tests were performed. Data acquisition was made with Instron software (Bluehill 3.0). For the wiggling mode, a stepper motor (two-phase Mercury motor with 1.8-degree step angle, and a holding torque of 2.3 kg-cm) was used. Tail samples were mounted on the stepper motor using the body mount and was wiggled for 10 s at various sweep angles and wiggling frequencies. The sweep angle and frequency were recorded at the event of full tail breakage for the microinterlocked and released microinterlock cases, which was later analyzed with the simulation results.

To demonstrate the tunable adhesion of the sample tail on a freely moving robot, we utilized the platform provided by the OWI KINGII Dragon Robot Kit, which included the leg movements as well as the base of the robot body. On this base, the following parts were integrated: a stepper motor, a stepper motor driver, a controller (Arduino nano), a proximity sensor, and a top casing cover. The stepper motor provided the wiggling motion of the tail with controlled amplitude and frequency once the proximity sensor was triggered. The pressure pump (Elveflow®) was connected to the PDMS patches via soft tubing to activate the releasing of the microinterlocks pneumatically while crawling.

2.5. Cohesive zone modeling

A cohesive zone modeling study among the three cases (planar, microinterlocked with and without the subsurface microchannel) was performed using Abaqus® Standard 6.16 [28–30]. The shapes and sizes of microinterlocks were set according to the experimental samples. To determine the cohesive and damage behavior, our recent study [7] was used where the penalty stiffness recorded was 0.025 N mm^{-3} in both the normal and shear directions. Furthermore, the damage criterion chosen was the maximum nominal stress (0.000 24 N mm^{-2}) in normal only and the other two mutually perpendicular shear directions. Moreover, the damage evolution criterion chosen was

energy (0.00024 N mm^{-1}) with exponential softening, including the Benzeggah-Kenane mode-mixity criterion (0.01 mode-mixity ratio, normal to shear). The material properties of PDMS (10:1 curing ratio), with a density of 960 kg m^{-3}, Young's modulus of 1.16 MPa, and Poisson's ratio of 0.49, were determined as per the tensile characterization using ASTM D412 type C samples [7]. The same properties were used for all modeling studies. The interfacial assembly and surface to surface interaction properties consisted of tangential behavior with a friction coefficient of 1.63 [7]. For the normal behavior contact interaction, a hard contact pressure overclosure and a default constraint enforcement method were used while allowing separation after contact.

The elements consisted of a four-node bilinear plane strain quadrilateral hybrid constant pressure (CPE4H). The global model's boundary condition comprised of the encastre condition on the top edge of the body part. The bottom of the tail was displaced 5 mm longitudinally. For submodels 1 and 2, only the relevant partitioned part was kept in the assembly module while the rest of the partitions were deleted. Finally, the boundary conditions were imparted to the appropriate partitioned edges from the associated previous global model. This was done using the submodel boundary conditions arrangement, where global model boundary conditions can be translated to the submodels concerning the relevant boundary edges. No automatic contact controls and stabilization were imparted for the contact interaction in the global model due to the coarse mesh nature. However, at the submodel level, the automatic contact controls and stabilization were kept in operation for the convergence [7], resulting in negligible interference of the stabilization and dissipation energies with the total strain energy.
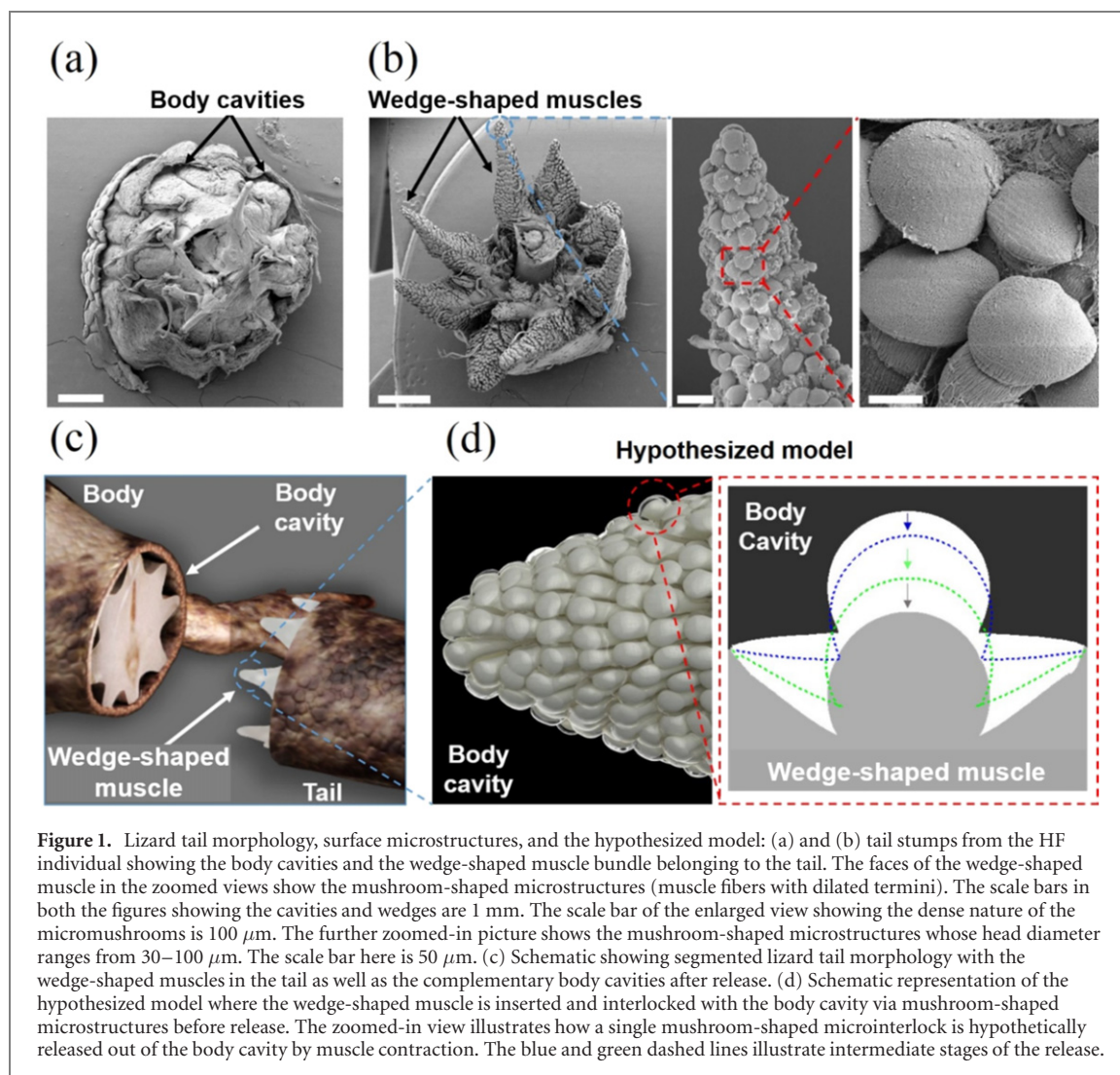
3. Lizard tail model

As a single organ, the lizard (*Hemidactylus flaviviridis*, HF) tail is found to be segmented and precut in nature, where each tail segment is connected with the other like a plug and socket joint [25]. The connections between these joints are made via wedge-shaped muscle bundles and the complementary body cavities (lined with layers of connective tissue, myosepta). The body cavities can be seen in the post-fracture SEM image, figure 1(a). The wedge-shaped muscle bundles, as shown in figure 1(b), were circumferentially arranged (total eight wedges, in two ventral, four lateral, and two dorsal directions). Due to the form-based macrointerlocking between the body cavities and the wedge-shaped muscle bundles, the faces of these wedges constituted the fracture planes. Furthermore, the SEM analysis of the fracture planes showed highly dense mushroom-shaped structures (bulged out distal ends of muscle

fibers) ranging from 30–80 μm in diameter, seen in zoomed-in views of figure 1(b). In other lizard species, *Cyrtopodion scabrum* (CS, Gekkonidae) as well as in *Acanthodactylus schmidti* (AS, Lacertidae), we also observed similar mushroom-shaped microstructures confirming the previous findings [25, 31]. Since the faces of these wedge-shaped muscle bundles constituted predetermined fracture regions [25] in an intact tail, under the action of critical stress induced by the predator's grasp, the tail is susceptible to rupture along these regions where a crack would initiate and propagate catastrophically, causing the total separation. Hence, tail autotomy can be regarded as a subject of interfacial fracture with predetermined fracture regions [32], as schematically shown in figure 1(c). To attach the tail as firmly as possible despite the presence of fracture planes, we hypothesized that the mushroom-shaped microstructures on the wedge-shaped muscle would act as biological microinterlocks to the counter body cavity, as shown schematically in figure 1(d). However, if needed in case of a predator's attack, these microstructures (muscle fibers with dilated termini) would actuate in an orchestrated manner. This can be realized via muscle contraction that would break the microinterlocks with the body cavity. Subsequently, tail autotomy process can be facilitated by tail thrashing. Schematically single microinterlock release using muscle contraction is illustrated in the zoomed-in inset of figure 1(d) where the blue and green dashed lines illustrate intermediate stages of the release (see supplementary text 1 for detailed schematic of the release). In reality, the biological process of muscle contraction would involve a cascade of complex chemical and mechanotransductive signals transmitted to muscle fibers [25] which poses a formidable challenge for a biomimetic implementation. Thus, in this study, we focussed only on the mechanical aspect of the fracture process and built a simplified biomimetic tail model by using a tunable adhesion patch out of a soft elastomeric material that can be pneumatically actuated mimicking muscle contraction.

4. Experimental

The bioinspired tunable adhesion model was built using a PDMS patch containing 12 000 microbumps fabricated on an area of 14 × 16 mm^2 using soft lithography and thermal reflow techniques (see corresponding method section). The size of the microbumps was determined based on the estimated size of the 'mushroom-shaped' microstructures in figure 1(b). Here, we chose a simple optimized design for the microbumps where the angle with the horizontal contacting surface was 90 degrees. However, as per the lizard tail SEM findings, this angle might differ, which in turn can have an undercut [7]. In our recent work [7], we specifically studied this

Figure 1. Lizard tail morphology, surface microstructures, and the hypothesized model: (a) and (b) tail stumps from the HF individual showing the body cavities and the wedge-shaped muscle bundle belonging to the tail. The faces of the wedge-shaped muscle in the zoomed views show the mushroom-shaped microstructures (muscle fibers with dilated termini). The scale bars in both the figures showing the cavities and wedges are 1 mm. The scale bar of the enlarged view showing the dense nature of the micromushrooms is 100 μm. The further zoomed-in picture shows the mushroom-shaped microstructures whose head diameter ranges from 30–100 μm. The scale bar here is 50 μm. (c) Schematic showing segmented lizard tail morphology with the wedge-shaped muscles in the tail as well as the complementary body cavities after release. (d) Schematic representation of the hypothesized model where the wedge-shaped muscle is inserted and interlocked with the body cavity via mushroom-shaped microstructures before release. The zoomed-in view illustrates how a single mushroom-shaped microinterlock is hypothetically released out of the body cavity by muscle contraction. The blue and green dashed lines illustrate intermediate stages of the release.

aspect of undercut (with the undercut angle of ∼70 degrees) based fracture using PDMS hemispherical microstructures and recorded significant (1.2-fold) increase in the adhesion strength compared to the non-undercut case. However, in this study, we specifically kept our focus on biomimicking tunable fracture behavior of lizard tail autotomy with hemi-spherical microinterlocking structures with no undercut that can be actuated to release using pneumatic means.

Figure 2(a) shows the design of a biomimetic 3D printed tail and body as well as the intermediate connection made out of PDMS. Instead of multiple cone-shaped wedges inserted into the body cavities as found in the lizard tail, the body-tail attachment was simplified to a single V-shaped wedge. The intermediate connection was made of four layers, as shown in the exploded view of figure 2(a), where 1 corresponds to the complementary microgroove layer attached to the body, 2 the self-assembled silane monolayer, 3 the microbump layer and 4 the control layer containing a winding microchannel aligned with the microbumps' array of layer 3. Layer 3 and 4 are plasma-bonded and constituted the integrated actuable PDMS patch. The assembled PDMS patch in figure 2(b) shows a

100 μm thick microbump layer which was further decreased down to 50 μm for facile deflection and was used in all the subsequent experimental characterization (see supplementary text 1). The microchannels of the control layer were aligned directly underneath the array of microbumps to facilitate deflection of the microbump layer and release the microinterlocks under action of negative pressure of 1000 mbar (supplementary video 1 and supplementary video 2 show the actuation at the macro- and microscale). The computational simulation further validated the feasibility of pneumatic actuation-based microinterlock release using the negative pressure (see supplementary text 3 and supplementary video 3 for the computational simulation).

After the release and complete detachment, the post-fracture SEM showed cleanly separated microbumps and microgrooves with no sign of cohesive damage; see post-fracture results in figure 2(b). This clean interfacial detachment was possible due to the silanized monolayer on the PDMS bilayer patch before bonding with the body part via PDMS filling, indicated in layer 2 in figure 2(a), that predetermined the crack path's propagation. Hence, this method
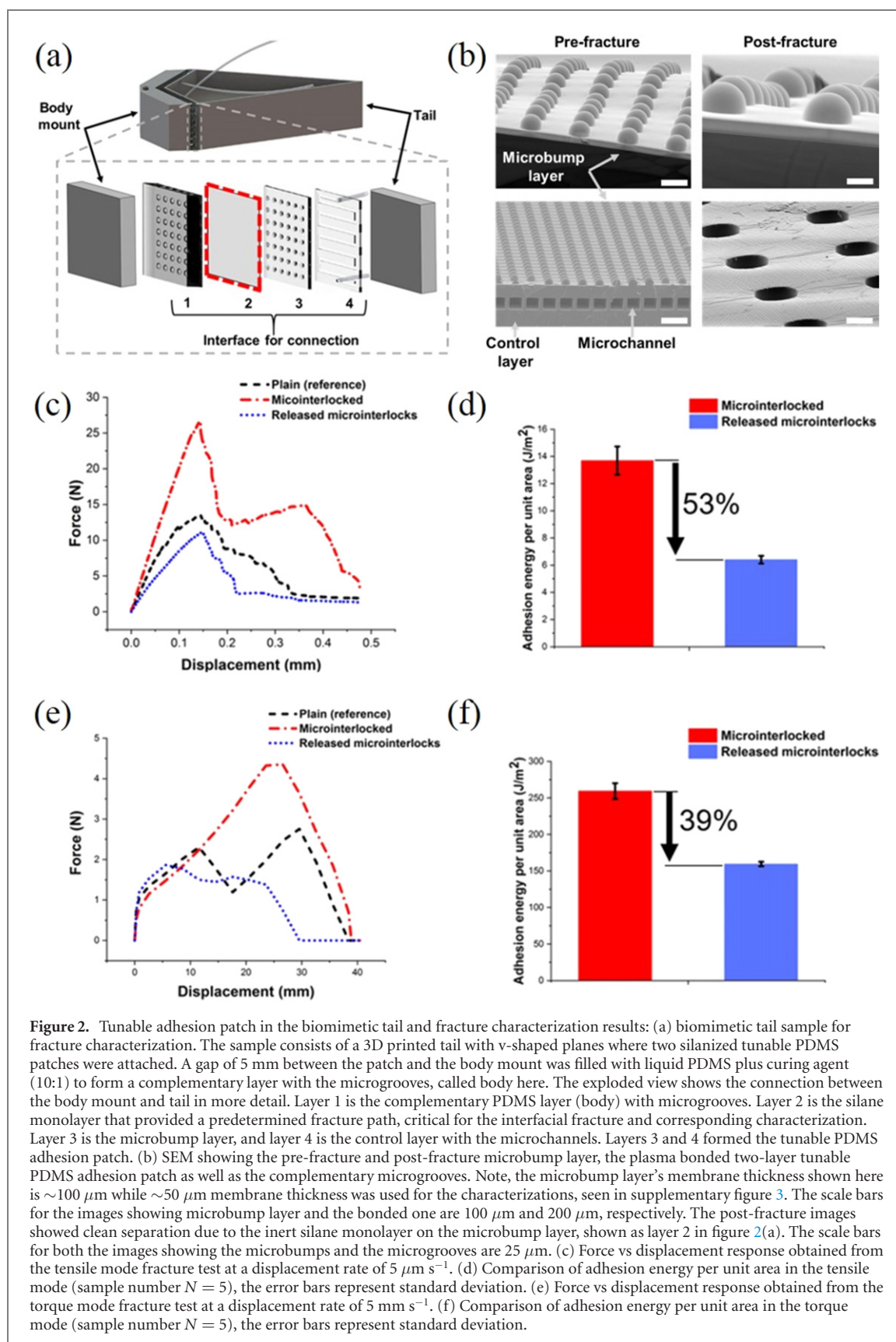
Figure 2. Tunable adhesion patch in the biomimetic tail and fracture characterization results: (a) biomimetic tail sample for fracture characterization. The sample consists of a 3D printed tail with v-shaped planes where two silanized tunable PDMS patches were attached. A gap of 5 mm between the patch and the body mount was filled with liquid PDMS plus curing agent (10:1) to form a complementary layer with the microgrooves, called body here. The exploded view shows the connection between the body mount and tail in more detail. Layer 1 is the complementary PDMS layer (body) with microgrooves. Layer 2 is the silane monolayer that provided a predetermined fracture path, critical for the interfacial fracture and corresponding characterization. Layer 3 is the microbump layer, and layer 4 is the control layer with the microchannels. Layers 3 and 4 formed the tunable PDMS adhesion patch. (b) SEM showing the pre-fracture and post-fracture microbump layer, the plasma bonded two-layer tunable PDMS adhesion patch as well as the complementary microgrooves. Note, the microbump layer's membrane thickness shown here is ~100 μm while ~50 μm membrane thickness was used for the characterizations, seen in supplementary figure 3. The scale bars for the images showing microbump layer and the bonded one are 100 μm and 200 μm, respectively. The post-fracture images showed clean separation due to the inert silane monolayer on the microbump layer, shown as layer 2 in figure 2(a). The scale bars for both the images showing the microbumps and the microgrooves are 25 μm. (c) Force vs displacement response obtained from the tensile mode fracture test at a displacement rate of 5 μm s^{-1}. (d) Comparison of adhesion energy per unit area in the tensile mode (sample number $N = 5$), the error bars represent standard deviation. (e) Force vs displacement response obtained from the torque mode fracture test at a displacement rate of 5 mm s^{-1}. (f) Comparison of adhesion energy per unit area in the torque mode (sample number $N = 5$), the error bars represent standard deviation.
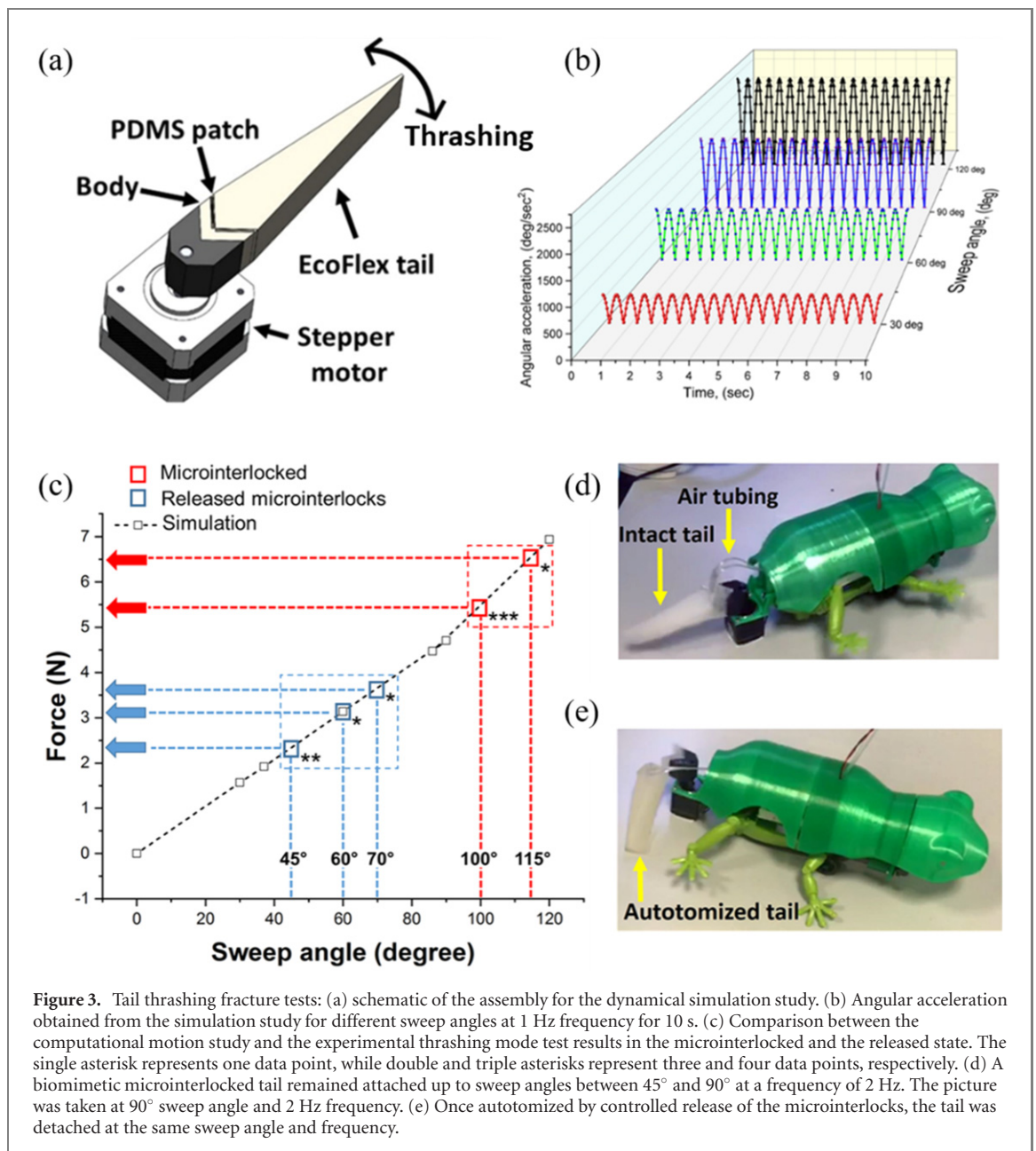
Figure 3. Tail thrashing fracture tests: (a) schematic of the assembly for the dynamical simulation study. (b) Angular acceleration obtained from the simulation study for different sweep angles at 1 Hz frequency for 10 s. (c) Comparison between the computational motion study and the experimental thrashing mode test results in the microinterlocked and the released state. The single asterisk represents one data point, while double and triple asterisks represent three and four data points, respectively. (d) A biomimetic microinterlocked tail remained attached up to sweep angles between 45° and 90° at a frequency of 2 Hz. The picture was taken at 90° sweep angle and 2 Hz frequency. (e) Once autotomized by controlled release of the microinterlocks, the tail was detached at the same sweep angle and frequency.

allowed accurate quantification by rendering the fracture highly interfacial without the cohesive bulk fracture based energy dissipation aspect interfering with the force–displacement response.

Tensile and torque fracture characterization tests were performed on the biomimetic tail to characterize interfacial fracture properties. In the tensile mode, the tail was deliberately grasped and pulled longitudinally, whereas, in the torque mode, the biomimetic tail sample was bent in the lateral direction to break. The fracture strength was characterized by the associated peak force, and the toughness was characterized by the associated adhesion energy (area under the force–displacement curve) per unit contact area. The force–displacement results from the tensile fracture tests at a displacement rate of 5 μm s^{-1} showed a considerable difference in the interfacial fracture strength and toughness between the tail samples,

as shown in figures 2(c) and (d) respectively. For the planar reference, a peak force of 13.48 N was recorded, while for the microinterlocked samples, the peak force was 26.60 N showing an increase of ∼97% compared to the planar reference surface. However, once the micromechanical interlocks were released by pneumatic actuation, the required peak force fell to 11.08 N, a decrease of ∼58% compared to the microinterlocked interface. In addition, a significant decline of ∼53% in the adhesion energy per unit area was measured between the microinterlocked and the released samples (figure 2(d)), indicating the significantly decreased ability of the interface to absorb strain energy because of the released microinterlocks.

Since the autotomy process primarily involves bending of the tail about a fulcrum (distance between predator's grasp and point of breakage), a torque fracture test (figure 2(e)) was also conducted. Here,

the characterization was performed using a soft biomimetic tail and body made in Ecoflex® 00-20 elastomer where the microinterlocks were between the PDMS patch (attached to the tail's V-shaped fracture planes) and the Ecoflex body part. The experiments were carried out at a displacement rate of 5 mm s^{-1} to mimic the high displacement rate of predator–prey interaction. The results indicated that, in the presence of microinterlocks, the peak force was significantly increased from 2.30 N to 4.47 N (∼94%) compared to the planar reference, as shown in figure 2(e). Furthermore, the tail was completely detached from the body part at a displacement of ∼39 mm. However, once the microscale interlocks were released by pneumatic actuation, the peak force dropped down to 1.92 N (∼57%) and the maximum displacement to ∼28 mm. Similarly, a significant decrease of the adhesion energy per unit area by 38% was measured between the microinterlocked and released tail samples (figure 2(f)).

To evaluate the fracture force generated during tail thrashing at the crack initiation site, the flexible tail's rotational mechanics was analyzed using Solidworks® motion study (figure 3(a)). First, angular acceleration (α) was evaluated and plotted for 10 s at different sweep angles (figure 3(b)). The measured maximum acceleration was utilized to calculate the maximum torque (T_{max}) and the maximum force experienced by the tail (supplementary text 4). For the sweep angle of 30°, 60°, 90° and 120°, the maximum force was found to be 1.56 N, 3.13 N, 4.70 N, and 6.94 N, respectively, and plotted in figure 3(c). Once the angle at which the tail broke was recorded, the fracture force was interpolated using the plot. Four out of five microinterlocked samples broke at 100°, and one at 115° within a thrashing force range of ∼5.5–6.5 N. However, once the interlocks were released, three out of five samples broke at 45°, while the others detached at 60° and 70° indicating a significantly lower thrashing force of ∼2.5–3.5 N. As a consolidated biomimetic demonstration of lizard tail autotomy, a tail sample was mounted on a freely moving lizard robot, as shown in figure 3(d). Without releasing the microinterlocks, the tail remained attached to the body at sweep angles varying from 45° to 90° and a thrashing frequency up to 2 Hz (supplementary video 4). However, after releasing the microinterlocks by pneumatic actuation, the tail broke almost instantaneously at 90° and 2 Hz, as shown in figure 3(e) (see supplementary video 5 for the movie).
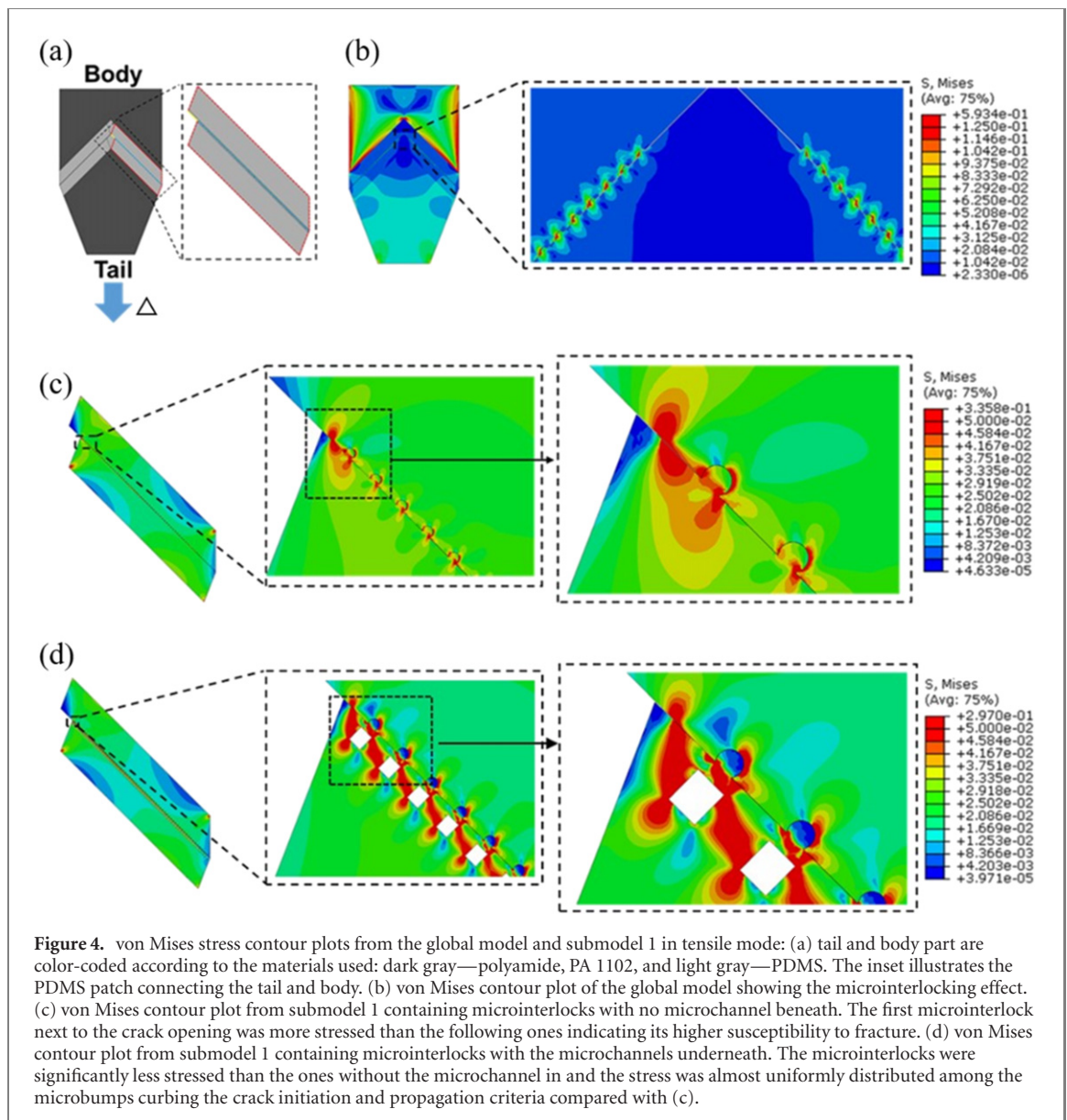
5. Computational

Using finite element modeling (FEM) and submodeling techniques [7], we evaluated the effect of the subsurface microchannels concerning fracture mechanics of the microinterlocked PDMS patch in tensile mode. Comparisons were made between the planar reference and microinterlocks without the microchannel cases. Figure 4(a) shows the global model in Abaqus® standard using cohesive zone modeling where the traction-separation parameters were taken from our recent study [7], critical for modeling the associated interfacial fracture behavior. The concerned parts were color-coded according to the materials used: dark gray—polyamide (PA 1102) representing the rigid body mount and tail and light gray—PDMS defining the soft interface. The inset illustrates the PDMS patch with microbumps and the body mount with complementary microgrooves in an interlocked condition. Figure 4(b) shows the von Mises stress map when the interlocked tail part was vertically displaced by $\Delta = 5$ mm along the tail axis. The notably severe contact interaction between the form-based complementary microstructures, seen in the related contour plot. More details regarding the meshed global model and submodel 1 and the corresponding energy comparison are explained in supplementary text 5.

Figure 4(c) shows the von Mises contour plot from submodel 1 for the microinterlocked interface with no microchannel beneath, and figure 4(d) shows the von Mises contour plot from submodel 1 with a microchannel underneath each microinterlock. The comparison between these two cases' contour plots for the same time step and boundary conditions indicated that with the microchannels, the interface showed more compliance than the interface without the microchannel. The compliant nature of the interface with the subsurface microchannels can be seen and compared in figures 4(c) and (d), where the microinterlock just after the pre-crack looks significantly less strained than the one without microchannels beneath, thus, rendering it vulnerable to crack initiation and propagation. Furthermore, for all microinterlocks, the comparison suggested a uniform stress distribution in the presence of microchannels than without, which marks stress concentration in the vicinity of the pre-crack approaching the first microinterlock. Moreover, the imparted compliance due to the microchannels deflected the high-stress regions away from the contact line where the crack is prone to initiate and propagate. Thus, the strategy of imparting a subsurface microchannel for pneumatic actuation of the microinterlocks kept the microinterlocks less strained and comparatively less prone to fracture initiation and propagation.

When performing single microinterlock level simulations using submodel 2, the results suggested complex contact interactions due to the associated microinterlock mode-mixity marked by simultaneous compressive and tensile zones [7, 33]. These interactions ultimately facilitated secondary and tertiary crack initiation and propagation (see supplementary videos 6 and 7 for the simulation without and

Figure 4. von Mises stress contour plots from the global model and submodel 1 in tensile mode: (a) tail and body part are color-coded according to the materials used: dark gray—polyamide, PA 1102, and light gray—PDMS. The inset illustrates the PDMS patch connecting the tail and body. (b) von Mises contour plot of the global model showing the microinterlocking effect. (c) von Mises contour plot from submodel 1 containing microinterlocks with no microchannel beneath. The first microinterlock next to the crack opening was more stressed than the following ones indicating its higher susceptibility to fracture. (d) von Mises contour plot from submodel 1 containing microinterlocks with the microchannels underneath. The microinterlocks were significantly less stressed than the ones without the microchannel in and the stress was almost uniformly distributed among the microbumps curbing the crack initiation and propagation criteria compared with (c).

with subsurface microchannel cases where the primary crack, secondary crack as well as tertiary crack were recorded). More details of the meshed submodel model 2 and the related convergence study can be seen in supplementary text 6). Figures 5(a)–(c) show the maximum principal contour plot for the planar (reference), a single microinterlock interface without and with microchannel underneath, respectively, at the same time step of 0.36 s. The comparison among the three cases suggested significantly less crack propagation in the presence of the microchannel compared with the other two cases because of the additional imparted compliance (see supplementary text 7 for the comparison during the secondary crack initiation event). Figures 5(d)–(f) show the maximum principal contour plot for the plain (reference), the microinterlocked interface without and with microchannel underneath, respectively, at the same final time step of 1 s. While the planar interface showed total separation, the interlocked ones remained attached.

The contact opening of the microinterlock with the microchannel was significantly less compared to the one without the microchannel because of its more compliant nature inducing a characteristic of a dissipative matrix for better energy absorption.

To quantify the fracture mechanics for these three considered cases, we compared strain energy dissipation rate (SEDR). The SEDR characterizes the strain energy that is dissipating from the crack tip normalized by the crack length. For the overall analysis, we also compared maximum contact opening (MCO) among them that did not involve any crack length normalization but was directly recorded from the cohesive zone model. SEDR was calculated from the single microinterlock fracture cases where the global total change in strain energy was estimated from the model, which was then normalized by the total change in interfacial separation length that was determined from the model at the end of the time step. SEDR decreased by 30%
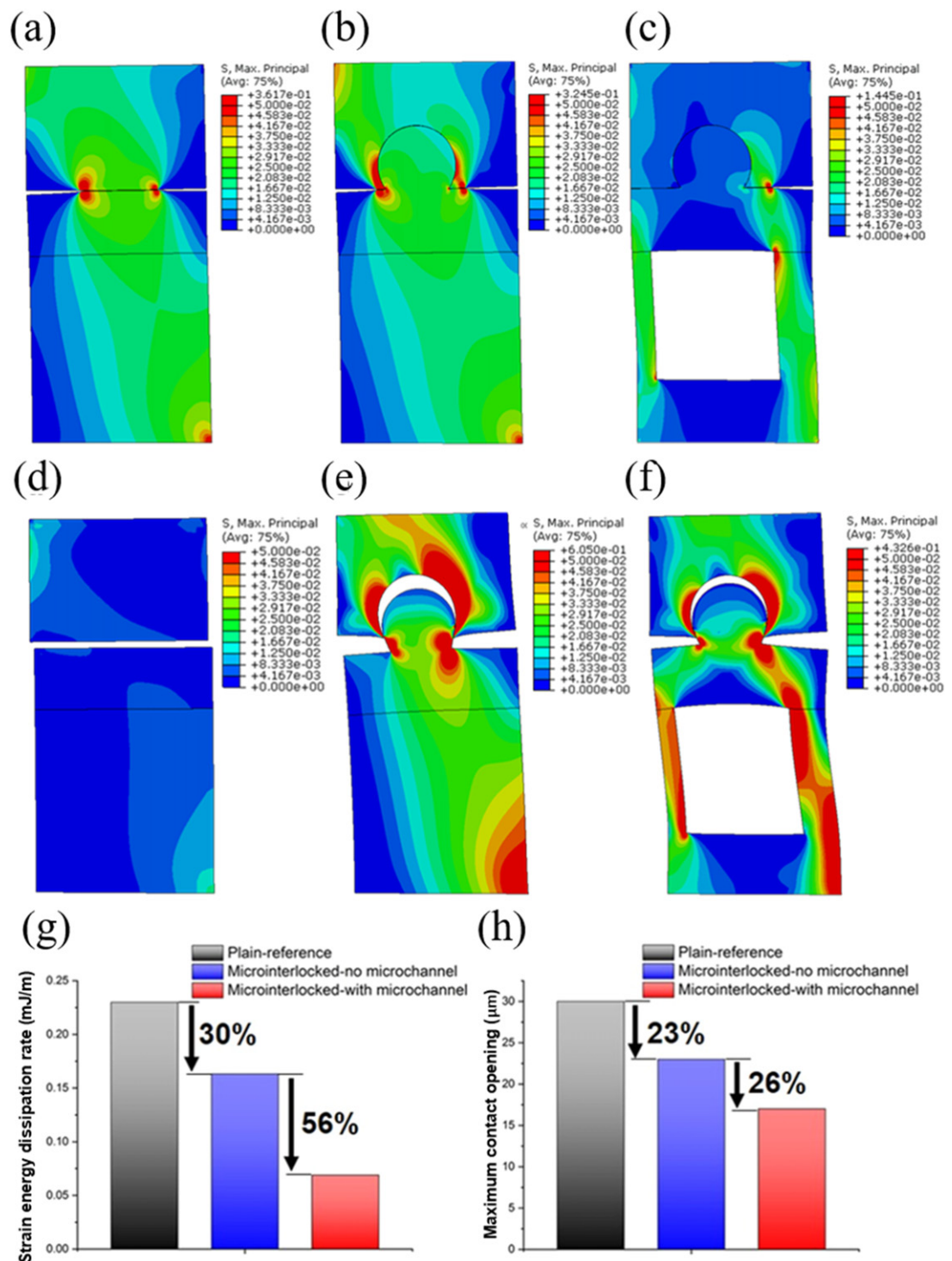
Figure 5. Simulation of fracture behavior of a single microinterlock in tensile mode with and without a microchannel in the control layer. (a) Maximum principal stress contour plot for submodel 2 containing plain interface (reference). (b) Maximum principal stress contour plot for the single microinterlock without a microchannel in the control layer. (c) Maximum principal stress contour plot for the single microinterlock with the microchannel in the control layer. (d)–(f) Maximum principal stress contour plots of the three cases at the final time step. The microinterlock with the microchannel in the control layer showed the least contact opening due to its compliant nature, acting as a dissipative matrix. (g) SEDRs for the three cases considered. Overall, the SEDR decreased by 86% when using the microinterlock with the microchannel in the control layer. (h) MCOs for the three cases. The MCO was reduced in total by 49% when using the microintelock with the microchannel in the control layer.

from the planar reference to the microinterlocked interface without the microchannel, as shown in figure 5(g). Furthermore, SEDR decreased by 56% with the microchannel. For MCO, a decrease of 23% was recorded between the planar reference

and the microinterlock with the microchannel, as shown in figure 5(h). Furthermore, a 26% decrease was recorded between the microinterlocks with and without microchannel where the former showed minimum contact opening (see details on the effect

of microbump size and its associated effect in supplementary text 8). The quantitative results underlined the benefit of integrating a subsurface microchannel to effectively alter the underlying fracture mechanics by rendering the interfacial system more compliant and energy absorbing in nature. This aspect of fracture augmentation using subsurface hollow interfaces has been reported by several previous bioinspired studies [34–38]. As a further advance in the field, our bioinspired approach combined the microinterlocking topology plus film-terminated ridge-channel hybrid synergistically to impart the highest possible interlayer fracture strength and toughness as well as simultaneous on-demand tunability.

6. Discussion

Bioinspired by lizard tail autotomy where a controlled rapid on-demand release of intact tail is seemingly possible, we proposed an approach to tunable interlayer adhesion between two soft layers by utilizing microinterlocking structures with an integrated microfluidic control layer underneath for pneumatic actuation.

Our biomimetic soft PDMS bilayer patch with the microbump layer on top of the control layer can be approximated as a film-terminated ridge-channel structure [35, 36], which has shown significant adhesion increase compared to the planar control layer due to augmented compliance [36, 39] plus the associated compliance induced crack trapping mechanism resulting from the curvature mismatch [34, 36] while the crack propagates. The adhesion augmentation using film-terminated microstructure has already been reported in several previous studies [34–42]. However, the topology of the film simply remained planar. Instead, our bioinspired approach utilized a combination of the microinterlocking topology plus film-terminated ridge-channel hybrid to impart the highest possible interlayer adhesion via the synergy. Thus, the control layer with the microchannel additionally enhanced the microinterlocking strategy [1–3, 5, 7] with the film terminated ridge-channel structure derived compliance impartment [34–38].

Once actuated, however, the adhesion switched instantly from high to low, as demonstrated experimentally. This hybrid approach using microinterlocking structures with the additional microchannel acting as a film-terminated ridge-channel structure enabled higher adhesion with on-demand tunability simultaneously. The displacement-controlled fracture experiments showed the macroscopic adherence behavior based on the microscopic interlocking conditions. The significant increase in the peak force (∼97% and ∼94% in tensile and torque mode, respectively, with respect to the planar reference surface) and adhesion energy per unit area (∼113% and

∼63% in tensile and torque mode, respectively, concerning the released microinterlocks condition) for the microinterlocked interface was attributed to the simultaneous strengthening and toughening due to the impinging crack propagation hindrance, mode-mixity and extended energy dissipation zone as well as intrinsic toughening mechanisms like crack deflection or kinking, C–G mechanism and stick-slip or microscale Lake–Thomas (L–T) [8, 43] effect. The physics of these aspects (called 'microinterlocking effect' here) were analyzed using the same interfacial system without pneumatic actuation in our recent work [7], where series of crack initiation and propagation mechanisms took place for every microinterlock one by one. Hence, the C–G and L–T effects took place altogether, increasing the interlayer adhesion significantly. The intermolecular adhesion effect (characterized by thermodynamic work of adhesion, a direct function of surface area [7]) remained negligible compared to microinterlocking effect both in tensile and torque mode (more details are given in supplementary text 9 and 10).

When the microinterlocks were released on-demand by pneumatic actuation, the peak force dropped by ∼58% and ∼57% in tensile and torque mode, respectively, with respect to the microinterlocked interface. The adhesion energy per unit area decreased by ∼53% and ∼38% in tensile and torque mode, respectively, with respect to the microinterlocked interface. The orchestrated release of microinterlocks generated closely packed microvoids that acted as stress concentration zones, and subsequent stress amplification and coalescences between the vicinal voids led to the rapid propagation of the crack. The tail thrashing experiment further validated the tunable adhesion of our biomimetic soft bilayer patch under dynamic conditions where sturdy connection under microinterlocked conditions and rapid detachment resulting from released microinterlock conditions were observed.

The FEM and CZM study on the microinterlock with and without microchannel control layer further elucidated the benefits of our soft bilayer patch in augmenting the fracture properties. A decrease of SEDR by 30% for the microinterlocked case without the subsurface microchannel indicated the benefit of having microinterlocking regime to effectively retain strain energy within the system. A further decrease of SEDR by 50% in the case of the microinterlocked interface with the subsurface microchannel was attributed to the compliant nature of the interface that was imparted due to the presence of the subsurface microchannel. Similarly, the MCO data clearly suggested significantly less contact opening between the microinterlocked interface without and with the microchannel by 26%, highlighting the advantages of the subsurface microchannel that enhanced the fracture properties (SEDR and MCO) by rendering the interface more compliant as a dissipative matrix.

As for the reversibility of microinterlock-based adhesion post delamination, the perfect registry of microbumps in the complementary microgrooves, when put back together, as in 'crack healing,' is expected to be compromised, resulting from inevitable misalignment. Thus, the reusability aspect of the presented engineered interface is limited and the subject of future work.

Some of the major differences between the biological and proposed bioinspired approaches were the shape, size, and density of microbumps. Especially, the actuation mechanism in the biological system is far more sophisticated [44] than the one used in the study, possibly by deploying a cascade of electrical, mechanical, and chemical processes to decrease the size of microstructures by rapid muscle contraction and release. Yet, this study can provide potential blueprints for future tunable adhesion systems where overarching mechanisms related to muscle contraction coupled with pre-stressed interfacial adhesion systems can be studied. We envision that this bioinspired hybrid approach towards tunable adhesion based on the microchannel controlled film-terminated microinterlocking strategy could find its use in fields such as bioinspired adhesives [45] and skin graft applications [46], soft robotics [47] and prosthetics [48], stretchable electronic skins [3, 49], tissue engineering [50, 51], conformal healthcare and organ machine interface [3].

7. Conclusions

In this paper, we presented a bioinspired approach to tunable adhesion between soft tissue layers using pneumatically-actuated microinterlocking structures in a soft elastomeric material (PDMS); and emulated interfacial fracture behavior of lizard tail autotomy. The hemispherical microinterlocks in the upper layer of the PDMS patch allowed firm attachment of the tail to the body. The significant 2.7-fold and three-fold increase in the peak force and adhesion energy per unit area, respectively, for the microinterlocked interface, was attributed to the simultaneous strengthening and toughening due to the enhanced crack propagation hindrance, mode-mixity, and extended energy dissipation zone as well as intrinsic toughening mechanisms like Cook–Gordon mechanism and Lake–Thomas effect. Furthermore, the microchannels in the control layer additionally enhanced the adhesion functioning as film-terminated microchannel-ridge structures that rendered the interface more compliant as a dissipative matrix.

However, once the microinterlocks were pneumatically released, mimicking muscle contraction, the peak force and adhesion energy per unit area decreased significantly by ∼50% enabling facile tail detachment. Finally and most likely, a first-ever biomimetic lizard tail mounted on a moving robot

that recapitulated on-demand quick release of the tail was demonstrated, validating the hypothesis. Overall, our soft patch allowed effective microinterlocking with the possibility of an orchestrated on-demand release of the microinterlocks, thereby altering the interlayer adhesion behavior of the patch for tunable adhesion. Thus, our work demonstrates a leap forward in building a tunable adhesion between soft layers with actuable microinterlocking structures and understanding the associated interfacial fracture behavior. This new bioinspired hybrid approach towards tunable adhesiveness based on the microchannel controlled film-terminated microinterlocking strategy could find its relevant use in fields such as soft robotics, electronic skins, bioadhesives, and prosthetic applications.

Data availability statement

All data that support the findings of this study are included within the article (and any supplementary files).

Conflict of interest

Authors declare that they have no competing interests.

Data and materials availability

All data and materials are available in the main manuscript and the supplementary manuscript.

Ethical statement

The research was approved by Institutional Animal Care and Use Committee (IACUC) and Environmental Agency Abu Dhabi, and the national or international standards were complied with.

Authors' contributions

The conceptualization, hypothesis and supervision was given by YS. The design of experiments, biomimetic design of tail and body parts, performance of experiments, simulation studies, data analysis and paper writing was done by NS. Ideas regarding Abaqus® simulation, and data analysis ideas were given CS. Fabrication of the photoresist master was done by AO.

Acknowledgments

ORCID iDs

Navajit S Baban ⬚ https://orcid.org/0000-0001-5804-0070

Yong-Ak Song ⬚ https://orcid.org/0000-0001-8066-2933

References

[1] Rivera J *et al* 2020 Toughening mechanisms of the elytra of the diabolical ironclad beetle *Nature* **586** 543–8

[2] Huang W, Restrepo D, Jung J Y, Su F Y, Liu Z, Ritchie R O, McKittrick J, Zavattieri P and Kisailus D 2019 Multiscale toughening mechanisms in biological materials and bioinspired designs *Adv. Mater.* **31** 1901561

[3] Zhu M, Zhang F and Chen X 2020 Bioinspired mechanically interlocking structures *Small Struct.* **1** 2000045

[4] Dunlop J W C, Weinkamer R and Fratzl P 2011 Artful interfaces within biological materials *Mater. Today* **14** 70–8

[5] Liu Z, Zhang Z and Ritchie R O 2020 Interfacial toughening effect of suture structures *Acta Biomater.* **102** 75–82

[6] Cordisco F, Zavattieri P D, Hector L G and Bower A F 2014 On the mechanics of sinusoidal interfaces between dissimilar elastic-plastic solids subject to dominant mode I *Eng. Fract. Mech.* **131** 38–57

[7] Baban N S, Orozaliev A, Stubbs C J and Song Y A 2020 Understanding interfacial fracture behavior between microinterlocked soft layers using physics-based cohesive zone modeling *Phys. Rev. E* **102** 012801

[8] Li Q, Zhang P, Yang C, Duan H and Hong W 2021 Switchable adhesion between hydrogels by wrinkling *Extreme Mechanics Letters* **43** 101193

[9] Malik I A, Mirkhalaf M and Barthelat F 2017 Bio-inspired 'jigsaw'-like interlocking sutures: modeling, optimization, 3D printing and testing *J. Mech. Phys. Solids* **102** 224–38

[10] Ritchie R O 2011 The conflicts between strength and toughness *Nat. Mater.* **10** 817–22

[11] Cordisco F A, Zavattieri P D, Hector L G and Carlson B E 2016 Mode I fracture along adhesively bonded sinusoidal interfaces *Int. J. Solids Struct.* **83** 45–64

[12] Pramanik S, Cherusseri J, Baban N S, Sowntharya L and Kar K K 2017 Metal matrix composites: theory, techniques, and applications *Composite Materials: Processing, Applications, Characterizations* (Berlin: Springer) pp 369–411

[13] Reddy S, Arzt E and del Campo A 2007 Bioinspired surfaces with switchable adhesion *Adv. Mater.* **19** 3833–7

[14] Barreau V, Hensel R, Guimard N K, Ghatak A, McMeeking R M and Arzt E 2016 Fibrillar elastomeric micropatterns

create tunable adhesion even to rough surfaces *Adv. Funct. Mater.* **26** 4687–94

[15] Tan D, Wang X, Liu Q, Shi K, Yang B, Liu S, Wu Z S and Xue L 2019 Switchable adhesion of micropillar adhesive on rough surfaces *Small* **15** 1904248

[16] Wang S, Luo H, Linghu C and Song J 2020 Elastic energy storage enabled magnetically actuated, Octopus-inspired smart adhesive *Adv. Funct. Mater.* **31** 2009217

[17] Frensemeier M, Kaiser J S, Frick C P, Schneider A S, Arzt E, Fertig R S and Kroner E 2015 Temperature-induced switchable adhesion using nickel–titanium–polydimethylsiloxane hybrid surfaces *Adv. Funct. Mater.* **25** 3013–21

[18] Geikowsky E and Aksak B 2020 Bioinspired fibrillar adhesives with shape-controlled off-center caps for switchable and directional adhesion *Bioinsp. Biomim.* **15** 56007

[19] Li X, Peng Z, Yang Y and Chen S 2019 Tunable adhesion of a bio-inspired micropillar arrayed surface actuated by a magnetic field *J. Appl. Mech.* **86** 011007

[20] Mohammadi Nasab A, Luo A, Sharifi S, Turner K T, Shan W, Shan W and Shan W 2020 Switchable adhesion via subsurface pressure modulation *ACS Appl. Mater. Interfaces* **12** 27717–25

[21] Deneke N, Chau A L and Davis C S 2020 Pressure tunable adhesion of rough elastomers *Soft Matter* **17** 863–9

[22] Yang S Y, O'Cearbhaill E D, Sisk G C, Park K M, Cho W K, Villiger M, Bouma B E, Pomahac B and Karp J M 2013 A bio-inspired swellable microneedle adhesive for mechanical interlocking with tissue *Nat. Commun.* **4** 1702

[23] Bateman P W and Fleming P A 2009 To cut a long tail short: a review of lizard caudal autotomy studies carried out over the last 20 years *J. Zool.* **277** 1–14

[24] Higham T E, Russell A P and Zani P A 2013 Integrative biology of tail autotomy in lizards *Physiol. Biochem. Zool.* **86** 603–10

[25] Sanggaard K W *et al* 2012 Unique structural features facilitate lizard tail autotomy *PLoS One* **7** e51803

[26] Baban N S *et al* 2018 Mechanistic approach to mimic lizard tail autotomy using deformable microstructures as biological interlock in the soft tissue *22nd Int. Conf. on Miniaturized Systems for Chemistry and Life Sciences, MicroTAS 2018* (Kaohsiung, Taiwan November 11–15, 2018) (Chemical and Biological Microsystems Society) pp 1670–1

[27] Chaturvedi N *et al* 2018 A single pressure pulse-actuated 3D-printed microfluidic tip for high throughput dispensing of C. elegans worms *22nd Int. Conf. on Miniaturized Systems for Chemistry and Life Sciences, MicroTAS 2018* (Kaohsiung, Taiwan November 11–15, 2018) (Chemical and Biological Microsystems Society) pp 1557–8

[28] Sofela S, Feng Y, Baban N S, Stubbs C J, Song Y-A and Wang W 2021 Biophysical phenotyping of C. elegans in a microfluidic chip for high-throughput drug screening *Micro and Nano Systems for Biophysical Studies of Cells and Small Organisms* ed X Liu and Y Sun (New York: Academic) pp 261–93

[29] Stubbs C J, Baban N S, Robertson D J, Alzube L and Cook D D 2018 Bending stress in plant stems: models and assumptions *Plant Biomechanics: From Structure to Function at Multiple Scales* ed A Gleitmann and J Gril (Berlin: Springer) pp 49–77

[30] Stubbs C J *et al* 2020 A generalized semi-automated rational design of micropillar arrays for mechanobiological studies *24th Int. Conf. on Miniaturized Systems for Chemistry and Life Sciences, MicroTAS 2020* (October 4–9) (Chemical and Biological Microsystems Society) pp 342–3

[31] Araújo T H, de Faria F P, Katchburian E and Haapalainen E F 2010 Ultrastructural changes in skeletal muscle of the tail of the lizard Hemidactylus mabouia immediately following autotomy *Acta Zool.* **91** 440–6

[32] Mohammed I K, Charalambides M N and Kinloch A J 2015 Modelling the interfacial peeling of pressure-sensitive adhesives *J. Non-Newton. Fluid Mech.* **222** 141–50

[33] Baban N S *et al* 2019 Bioinspired micromechanical interlocking structures for enhanced adherence between soft elastomeric layers *23rd Int. Conf. on Miniaturized Systems for Chemistry and Life Sciences, MicroTAS 2019* (Basel, Switzerland October 27 – November 1, 2019) (Chemical and Biological Microsystems Society) pp 1130–1

[34] Morano C, Zavattieri P and Alfano M 2020 Tuning energy dissipation in damage tolerant bio-inspired interfaces *J. Mech. Phys. Solids* **141** 103965

[35] Wu H, Moyle N, Jagota A, Khripin C Y, Bremond F and Hui C-Y 2019 Crack propagation pattern and trapping mechanism of rolling a rigid cylinder on a periodically structured surface *Extreme Mechanics Letters* **29** 100475

[36] He Z, Moyle N M, Hui C-Y, Levrard B and Jagota A 2017 Adhesion and friction enhancement of film-terminated structures against rough surfaces *Tribol. Lett.* **65** 161

[37] Majumder A, Sharma A and Ghatak A 2010 A bioinspired wet/dry microfluidic adhesive for aqueous environments *Langmuir* **26** 521–5

[38] Glassmaker N J, Jagota A, Hui C-Y, Noderer W L and Chaudhury M K 2007 Biologically inspired crack trapping for enhanced adhesion *Proc. Natl Acad. Sci.* **104** 10786–91

[39] Vajpayee S, Jagota A and Hui C-Y 2010 Adhesion of a fibrillar interface on wet and rough surfaces *J. Adhes.* **86** 39–61

[40] Ghareeb A and Elbanna A 2018 On the role of the plaque porous structure in mussel adhesion: implications for adhesion control using bulk patterning *J. Appl. Mech.* **85** 121003

[41] Majumder A, Ghatak A and Sharma A 2007 Microfluidic adhesion induced by subsurface microstructures *Science* **318** 258–61

[42] Ghareeb A and Elbanna A 2019 Extreme enhancement of interfacial adhesion by bulk patterning of sacrificial cuts *Extreme Mechanics Letters* **28** 22–30

[43] Chung J Y and Chaudhury M K 2005 Roles of discontinuities in bio-inspired adhesive pads *J. R. Soc., Interface* **2** 55–61

[44] Whitesides G M 2015 Bioinspiration: something for everyone *Interface Focus* **5** 20150031

[45] Carbone G and Pierro E 2013 A review of adhesion mechanisms of mushroom-shaped microstructured adhesives *Meccanica* **48** 1819–33

[46] Frost S J, Mawad D, Hook J and Lauto A 2016 Micro- and nanostructured biomaterials for sutureless tissue repair *Adv. Healthcare Mater.* **5** 401–14

[47] Trivedi D, Rahn C D, Kier W M and Walker I D 2008 Soft robotics: biological inspiration, state of the art, and future research *Appl. Bionics Biomech.* **5** 99–117

[48] Wu Y *et al* 2018 A skin-inspired tactile sensor for smart prosthetics *Sci. Robot.* **3** eaat0429

[49] Rodrigues D, Barbosa A I, Rebelo R, Kwon I K, Reis R L and Correlo V M 2020 Skin-integrated wearable systems and implantable biosensors: a comprehensive review *Biosensors* **10** 79

[50] Luu T U, Gott S C, Woo B W K, Rao M P and Liu W F 2015 Micro- and nanopatterned topographical cues for regulating macrophage cell shape and phenotype *ACS Appl. Mater. Interfaces* **7** 28665–72

[51] Qazi T H, Mooney D J, Pumberger M, Geißler S and Duda G N 2015 Biomaterials based strategies for skeletal muscle tissue engineering: existing technologies and future trends *Biomaterials* **53** 502–21